

Supporting Information

Oxalate Promoted Iron Dissolution of Hematite via Proton Coupled Electron Transfer

Guangming Zhan[†], Yumin Fang[†], Meng Zhang, Shiyu Cao, Tianyuan Xu, Cancan Ling, Huayu Gu,

Xiao Liu, and Lizhi Zhang**

Key Laboratory of Pesticide & Chemical Biology of Ministry of Education, Institute of
Environmental & Applied Chemistry, College of Chemistry, Central China Normal University,
Wuhan 430079, People's Republic of China

* Corresponding authors

E-mail: liuxiao71@mail.ccnu.edu.cn (Xiao Liu)

zhanglz@mail.ccnu.edu.cn (Lizhi Zhang)

CONTENTS

Text S1. Characterization of hematite samples	S4
Text S2. ATR-FTIR spectroscopy analysis	S4
Text S3. Electrochemical measurements	S5
Text S4. Adsorption isotherms	S5
Figure S1. Standard curve of oxalate with a concentration of 0.005 to 0.2 mmol L ⁻¹	S6
Figure S2. Standard curve of oxalate with a concentration of 0.2 to 4.0 mmol L ⁻¹	S6
Figure S3. Standard curve of Fe(II) with a concentration of 5 to 80 μmol L ⁻¹	S7
Figure S4. Standard curve of Fe(II) with a concentration of 0.08 to 1.2 mmol L ⁻¹	S7
Figure S5. Periodic model of HNPs {001} surface in aqueous solution	S8
Figure S6. XRD patterns and Raman spectra of the prepared HNPs	S8
Figure S7. The specific surface area of the prepared HNPs	S9
Figure S8. The XPS spectra of the prepared HNPs	S9
Figure S9. Linear fitting of HNPs dissolution at various pH	S10
Figure S10. The evolution of pH value during the HNPs dissolution	S10
Figure S11. Iron dissolution under Ar and Air condition	S11
Figure S12. Linear fitting of HNPs dissolution with various oxalate concentration	S11
Figure S13. Langmuir plot for the adsorption of oxalate by HNPs	S12
Figure S14. SEM and TEM images of HNPs iron dissolution	S12
Figure S15. Stretching modes of aqueous C ₂ O ₄ ²⁻	S13

Figure S16. Peak fitting of ATR-FTIR spectra	S13
Figure S17. Stretching modes of adsorbed $C_2O_4^{2-}$	S14
Figure S18. Optimized atomic configurations of various HNPs {001}	S14
Figure S19. The original structure of proton transfer process of adsorbed $HC_2O_4^-$	S15
Figure S20. The proton transfer process of adsorbed $HC_2O_4^-$	S15
Figure S21. The HNPs dissolution in H_2O and D_2O at pH 4.0	S16
Figure S22. The HNCs dissolution in H_2O and D_2O at pH 3.0	S16
Figure S23. The goethite and ferrihydrite dissolution in H_2O and D_2O at pH 3.0	S17
Figure S24. The Fe speciation as a function of pH	S17
Table S1. Iron dissolution and oxalate adsorption capacities at various pH	S18
Table S2. Iron dissolution and oxalate adsorption capacities at various oxalate concentration.....	S18
Table S3. IR frequencies of adsorbed oxalate on HNPs.....	S19

Text S1. Characterization of hematite samples.

The hematite nanoplates was characterized by powder X-ray diffraction measurements (XRD, D/Max-III A X-ray diffractometer, Cu K α radiation, $\lambda = 0.15418$ nm) and Raman spectrometer (DXR, Thermo) equipped with a 532 nm laser excitation source. The specific surface areas were determined by Brunauer-Emmett-Teller (BET) nitrogen adsorption isotherms with a micromeritics 3020 instrument. The chemical states of surface elements were measured by X-ray photoelectron spectroscopy (XPS, Perkin-Elmer PHI 5000C). The morphologies were recorded by scanning electron microscopy (SEM, JEOL 6700-F) and transmission electron microscopy (TEM, JEOL-2010).

Text S2. ATR-FTIR spectroscopy analysis.

ATR-FTIR spectroscopy were performed on a FTIR spectrometer (Nicolet iS50, Thermo) equipped with a diamond internal reflection unit and a mercury-cadmium-telluride (MCT) detector. First, 10 μ L of hematite suspension (4.0 g L⁻¹) was dropped onto the surface of diamond crystal, which was naturally dried to form a translucent film. And a background spectrum was collected through the average of 256 scans at the resolution of 4 cm⁻¹. Then, the oxalate solution was dropped into the hematite film surface for the immediate collection of infrared spectrum.

Text S3. Electrochemical measurements.

Open circuit potential analysis was performed in a two-electrode configuration in Na₂SO₄ electrolyte (0.05 mol L⁻¹) at 25 °C. A gold working electrode was pre-cleaned in acetone. 10 μL of hematite suspension (4.0 g L⁻¹) was dropped onto the gold electrode and dried at 50 °C for following open circuit potential measurements. Then, a standard Ag/AgCl reference electrode (filled with saturated KCl solution) was inserted in a Luggin capillary (filled with Na₂SO₄ electrolyte), which was assembled near the surface of working electrode to reduce the ohmic potential drops. The open circuit potential value was recorded by a computer-controlled electrochemical workstation (CHI-660D, Shanghai Chenghua, China). After the potential reached a steady state, a certain amount of oxalic solution was added into the solution while the open circuit potential was continuously measured during the adsorption process.

Text S4. Adsorption isotherms

The oxalate adsorption equilibrium was tested by using Langmuir isotherm model isotherm model. The linear form of Langmuir equation is written as eq 1.

$$1/q_e = 1/(K_L C_e) + 1/q_m \quad (1)$$

where C_e is the equilibrium concentration of oxalate (mmol L⁻¹), q_e is the amount of oxalate adsorbed per unit mass of the HNPs at equilibrium (mmol g⁻¹), q_m (mmol g⁻¹) is the maximum adsorption capacity, and K_L (L mmol⁻¹) is the equilibrium constant.

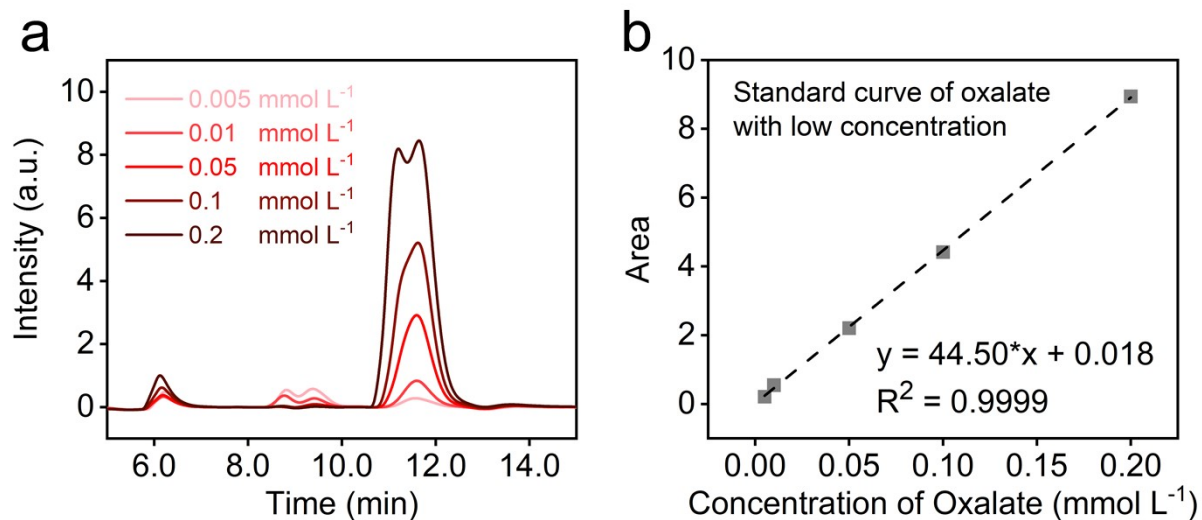


Figure S1. (a) The original data of anion exchange chromatography, and (b) fitted standard curve of oxalate with a concentration of 0.005 to 0.2 mmol L⁻¹.

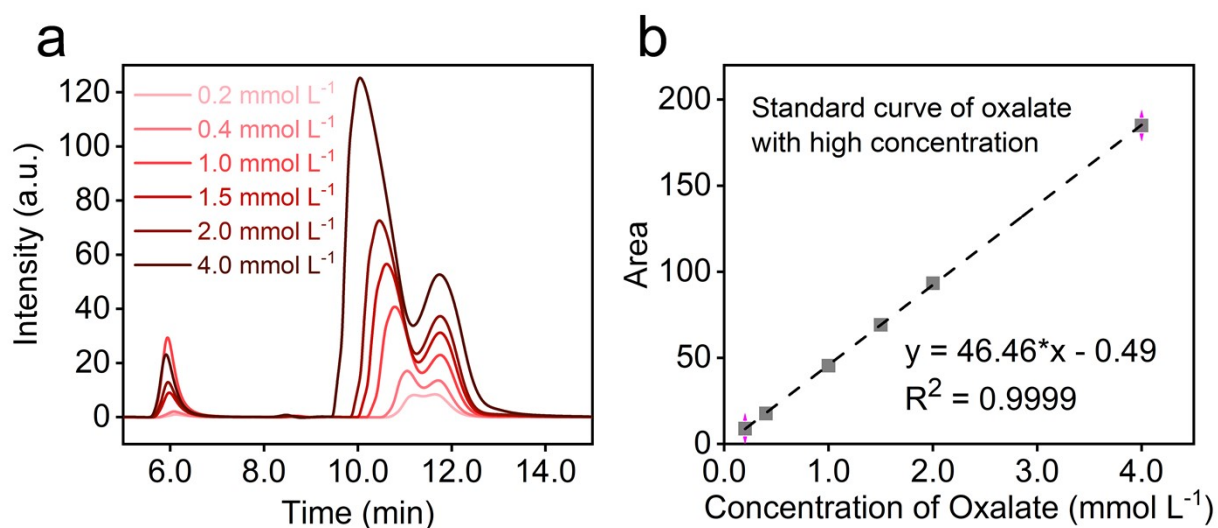


Figure S2. (a) The original data of anion exchange chromatography, and (b) fitted standard curve of oxalate with a concentration of 0.2 to 4.0 mmol L⁻¹.

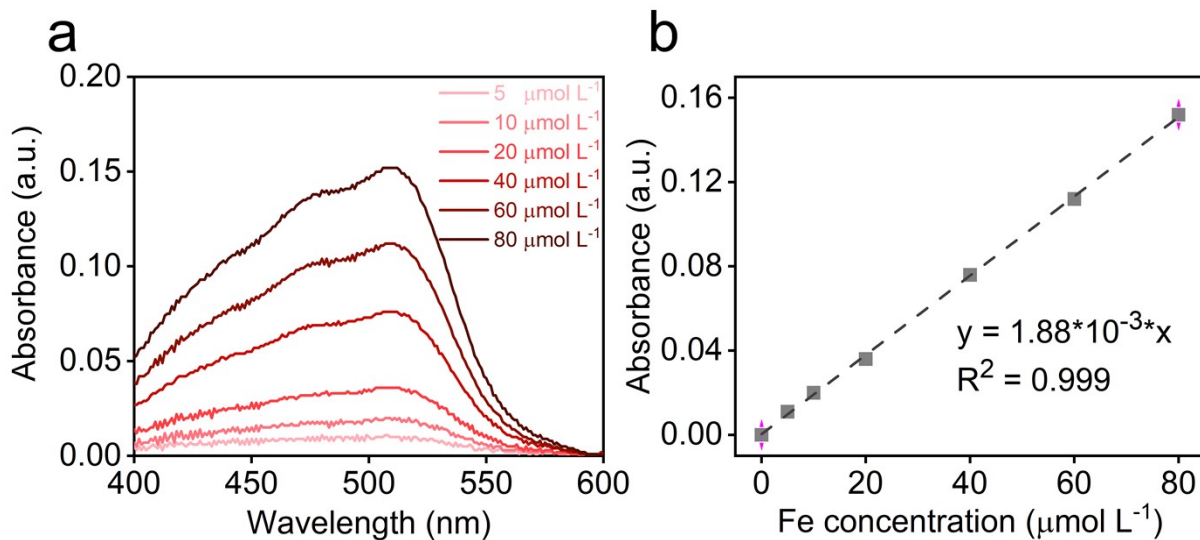


Figure S3. (a) The original data of UV-vis spectrophotometer, and (b) fitted standard curve of Fe(II) with a concentration of 5 to 80 $\mu\text{mol L}^{-1}$.

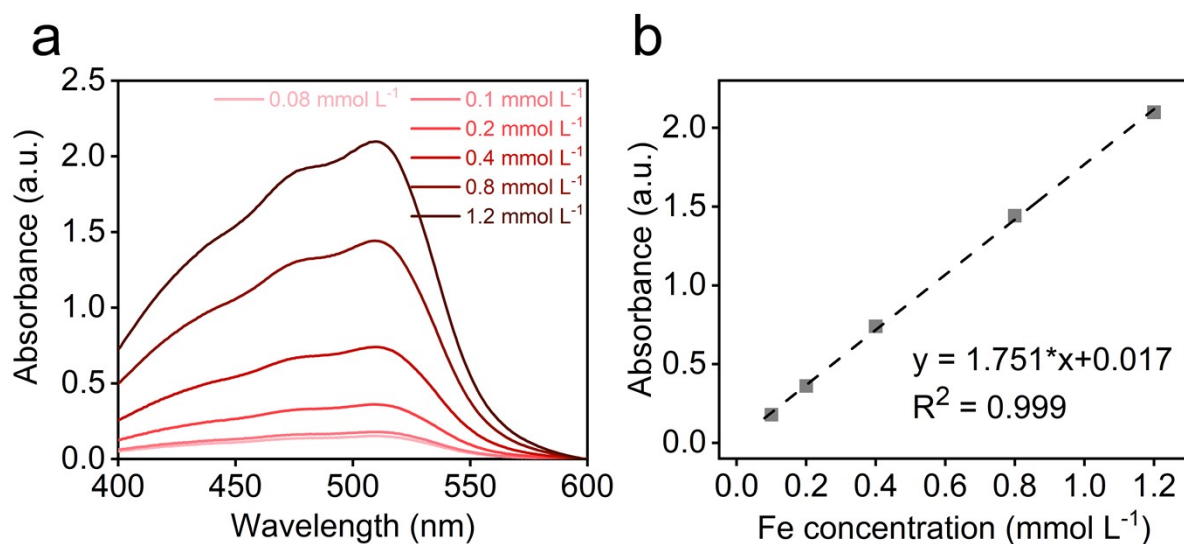


Figure S4. (a) The original data of UV-vis spectrophotometer, and (b) fitted standard curve of Fe(II) with a concentration of 0.08 to 1.2 mmol L^{-1} .

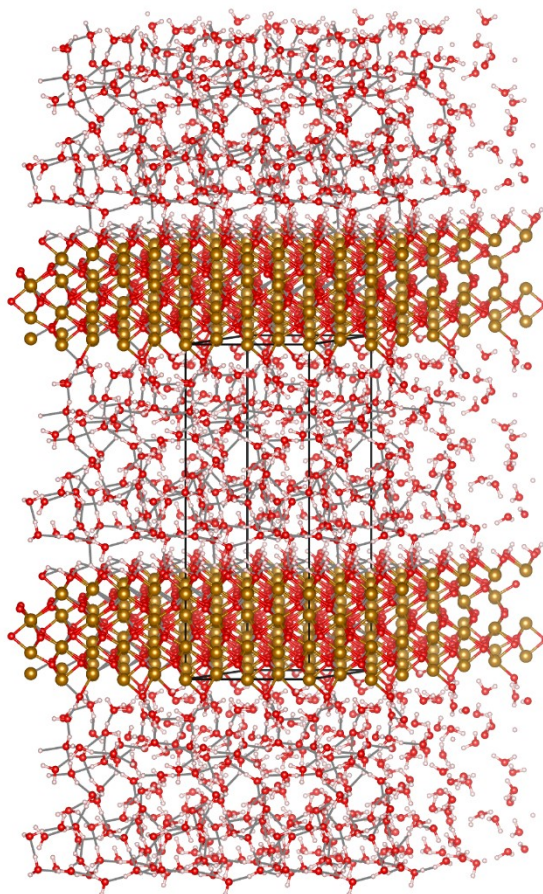


Figure S5. Periodic model of HNPs {001} surface in aqueous solution. The brown, red, gray, and white balls represent Fe, O, C, and H atoms, respectively.

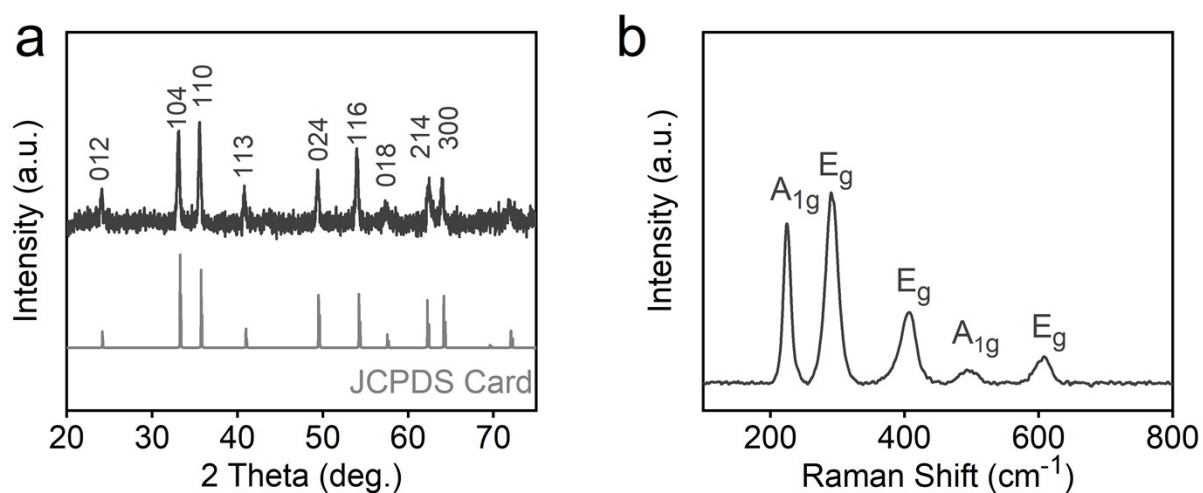


Figure S6. (a) The XRD patterns and (b) Raman spectra of the prepared HNPs. The XRD and Raman spectra revealed that the samples were crystalline α -Fe₂O₃ in rhombohedral hexagonal phase.

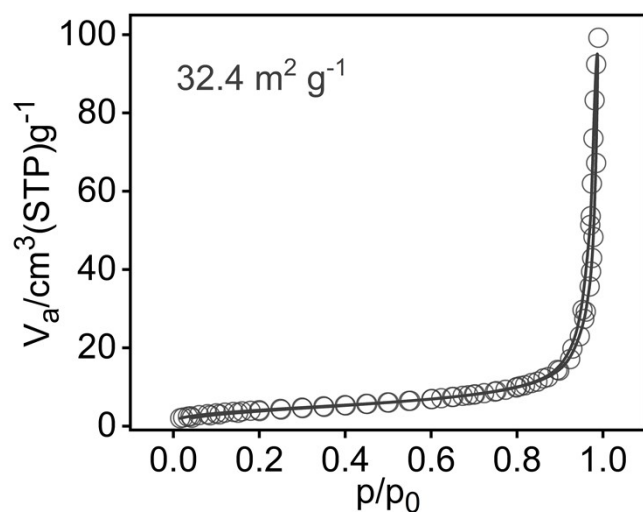


Figure S7. The specific surface area of the prepared HNPs was $32.4 \text{ m}^2 \text{ g}^{-1}$ as calculated from N_2 adsorption results.

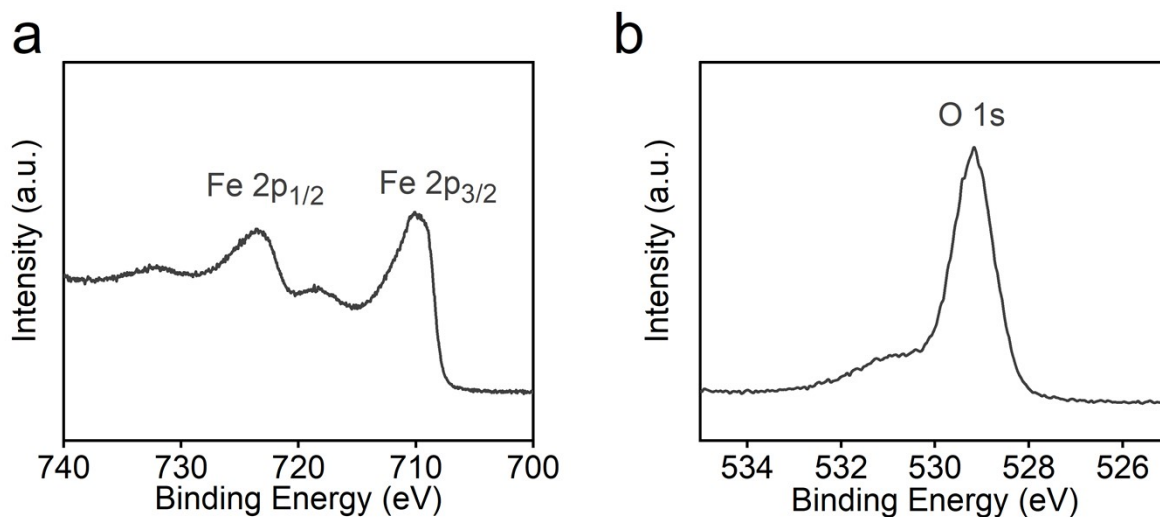


Figure S8. The XPS spectra of (a) Fe and (b) O of prepared HNPs. High-resolution Fe 2p and O 1s XPS spectra revealed that HNPs were not contaminated before oxalate adsorption.

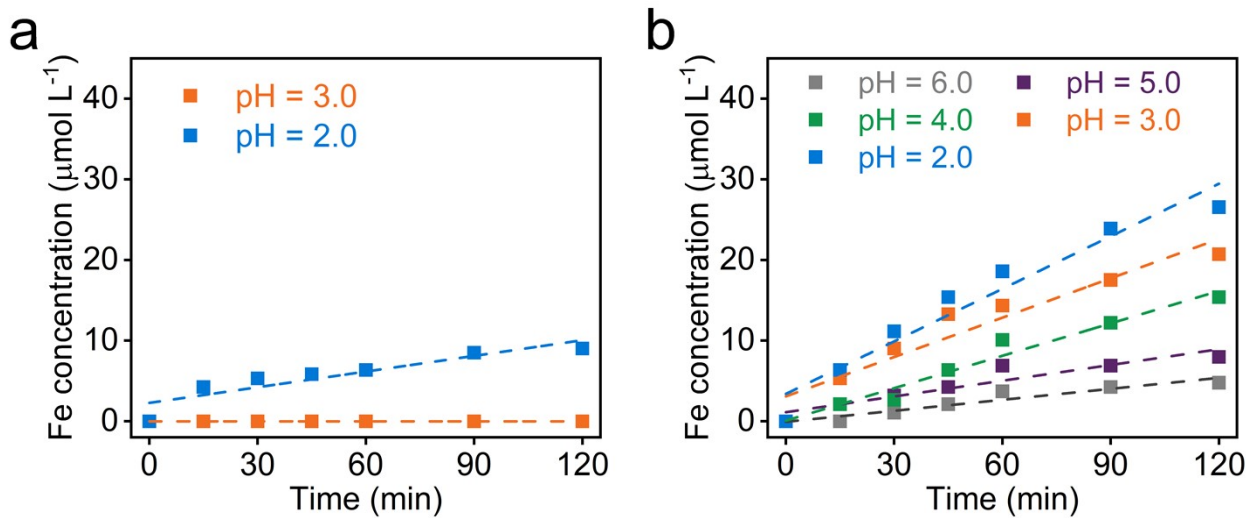


Figure S9. The linear fitting of HNPs dissolution (a) in the absence of oxalate and (b) with 1.0 mmol L^{-1} oxalate at various pH.

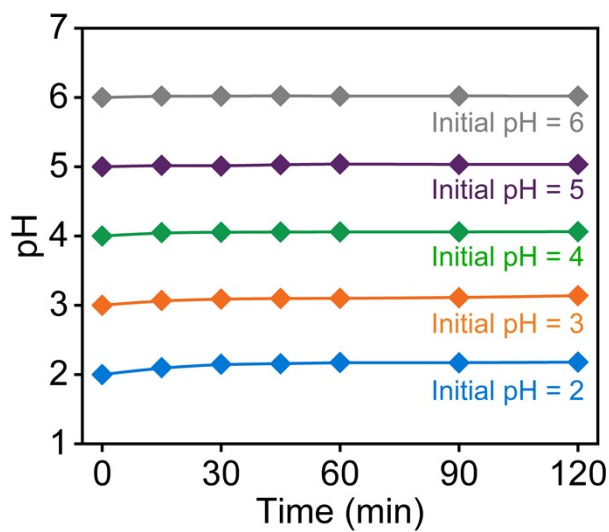


Figure S10. The evolution of pH value during the HNPs dissolution in 1.0 mmol L^{-1} oxalate solution under various initial pH.

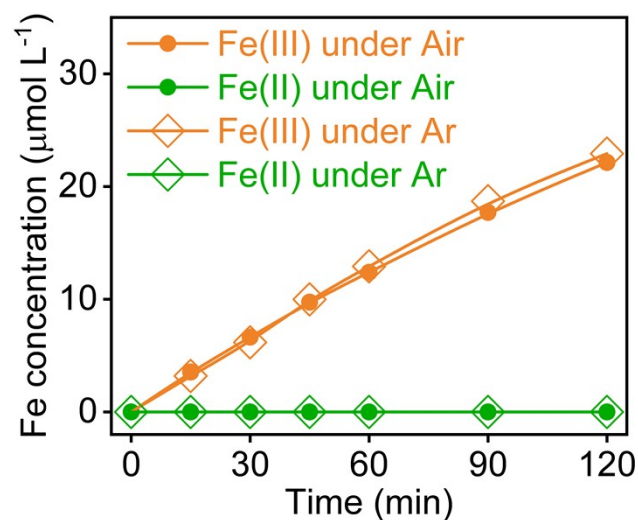


Figure S11. Iron dissolution of HNP {001} dissolution at pH 3.0 in the presence 1.0 mmol L^{-1} oxalate under Ar and Air condition. The hematite dissolution experiments were conducted in the absence of light, which is a non-reductive dissolution process, and the presence of Air and Ar almost has little effect on the iron dissolution.

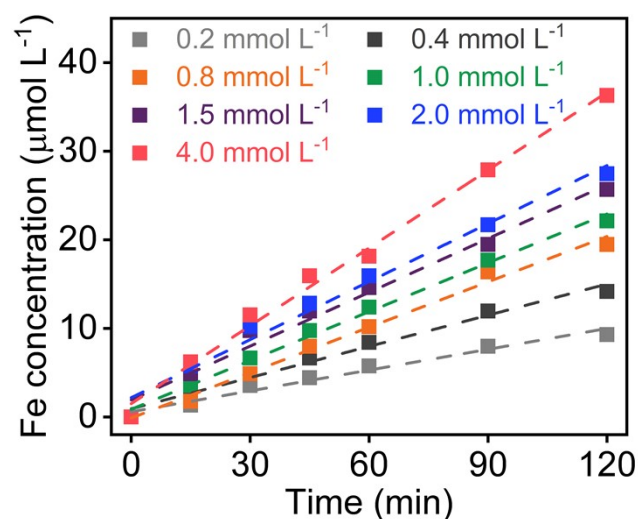


Figure S12. The linear fitting of HNP dissolution at pH 3.0 with various concentration of oxalate.

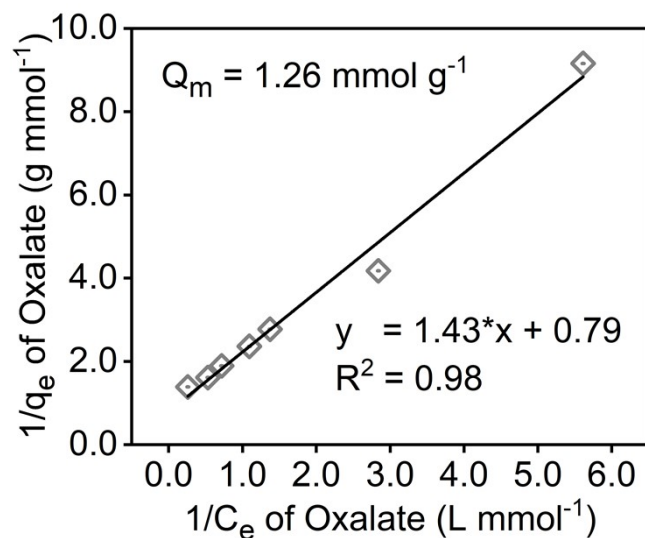


Figure S13. Langmuir plot for the adsorption of oxalate by HNPs at pH 3.0. The concentration of HNPs was 0.2 g L^{-1} . The initial oxalate concentrations ranged from 0.2 to 4.0 mmol L^{-1} . The calculated maximum oxalate adsorption capacity of HNPs was 1.26 mmol g^{-1} .

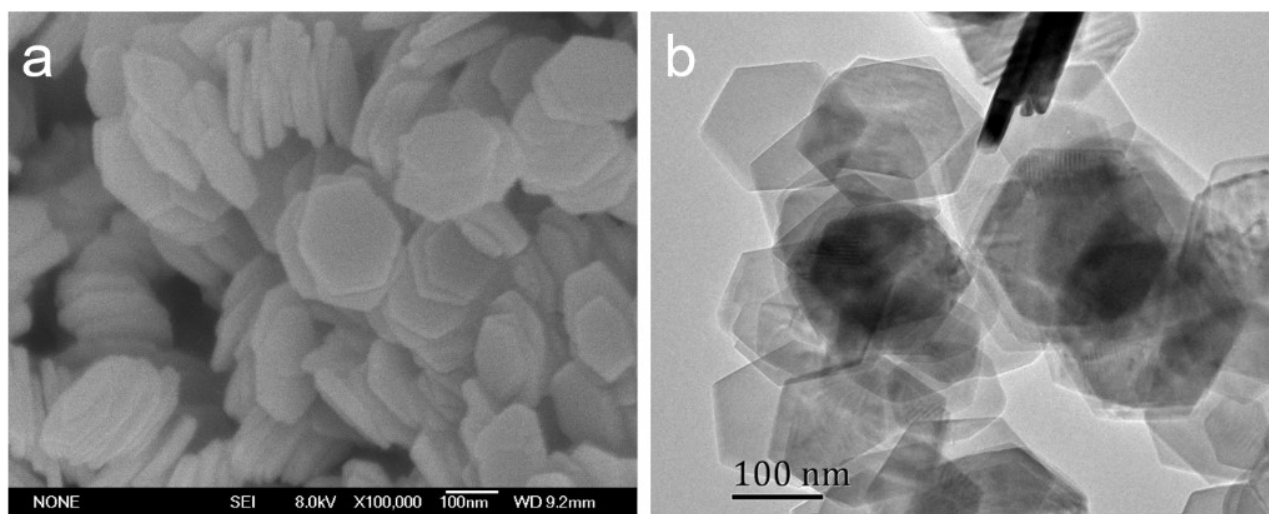


Figure S14. (a) SEM and (b) TEM images of HNPs {001} after 48 hours of iron dissolution at pH 3.0 in the presence of 1.0 mmol L^{-1} oxalate.

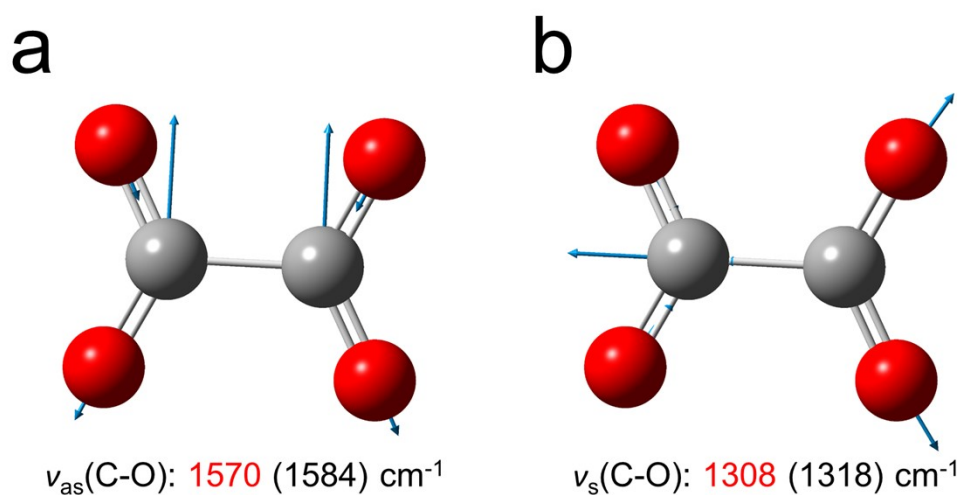


Figure S15. (a) Asymmetric $v_{as}(\text{C-O})$ and (b) symmetric $v_s(\text{C-O})$ stretching modes of aqueous $\text{C}_2\text{O}_4^{2-}$, and the observed frequencies (red) and simulated frequencies (black, bracket) of the stretching modes. The red and gray balls represent O and C atoms, respectively.

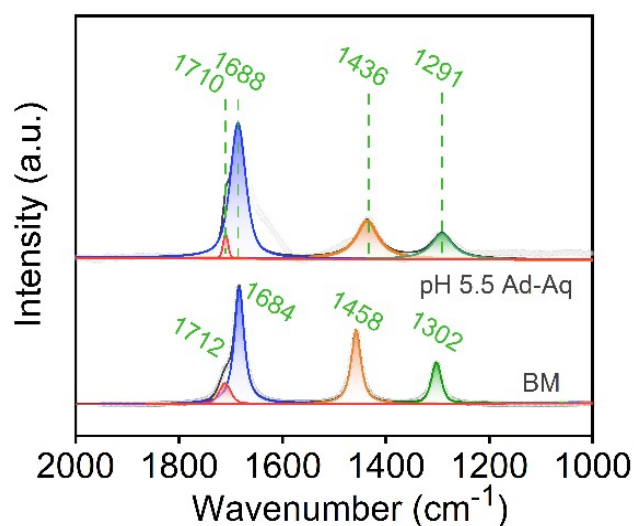


Figure S16. Peak fitting of ATR-FTIR spectra of oxalate adsorbed on HNPs under pH 5.5, and peak fitting of simulated FTIR spectra of oxalate in bidentate mononuclear adsorption configurations.

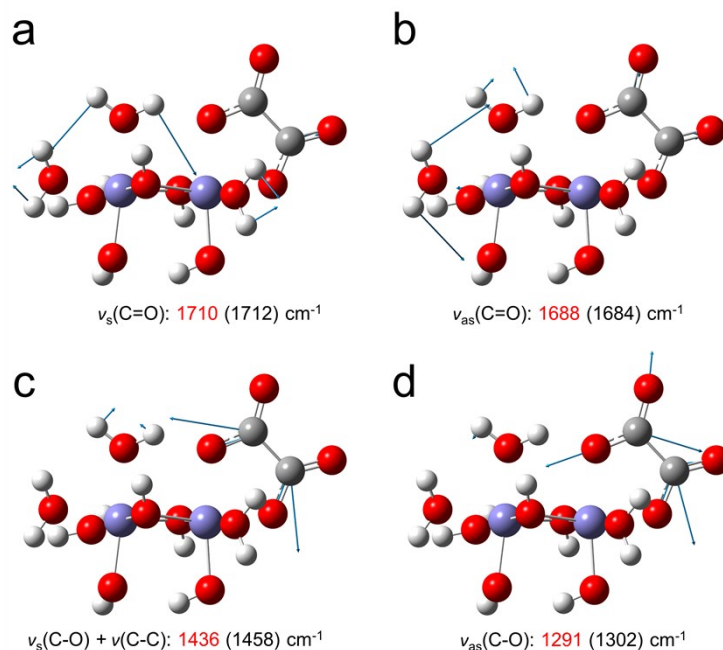


Figure S17. (a) $\nu_s(\text{C}=\text{O})$, (b) $\nu_{as}(\text{C}=\text{O})$, (c) $\nu_s(\text{C}-\text{O}) + \nu(\text{C}-\text{C})$ and (d) $\nu_{as}(\text{C}-\text{O})$ stretching modes of adsorbed oxalate of bidentate mononuclear configuration, and the observed frequencies (red) and simulated frequencies (black, bracket) of the stretching modes. The purple, red, gray, and white balls represent Fe, O, C, and H atoms, respectively.

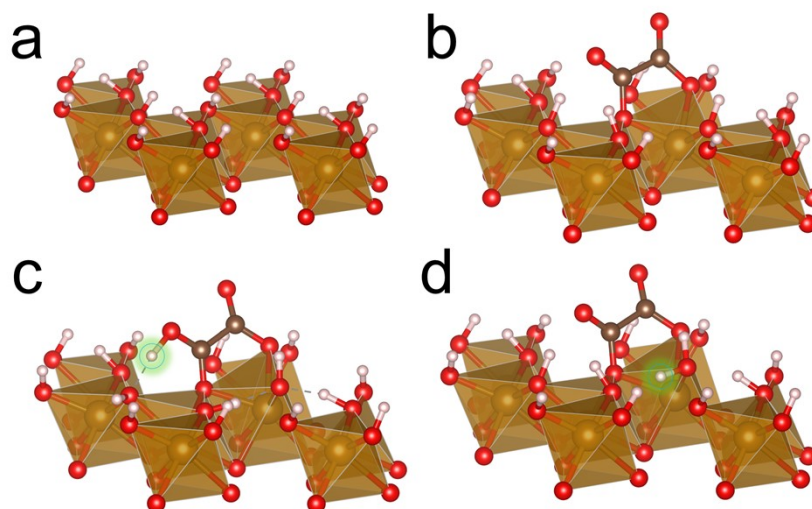


Figure S18. Optimized atomic configurations of hydroxyl terminated HNPs {001} surface (a) before and (b) after $\text{C}_2\text{O}_4^{2-}$ adsorption, and HC_2O_4^- adsorbed HNPs {001} surface (c) before and (d) after proton transfer. The brown polyhedron, red, gray, and white balls represent Fe, O, C, and H atoms, respectively.

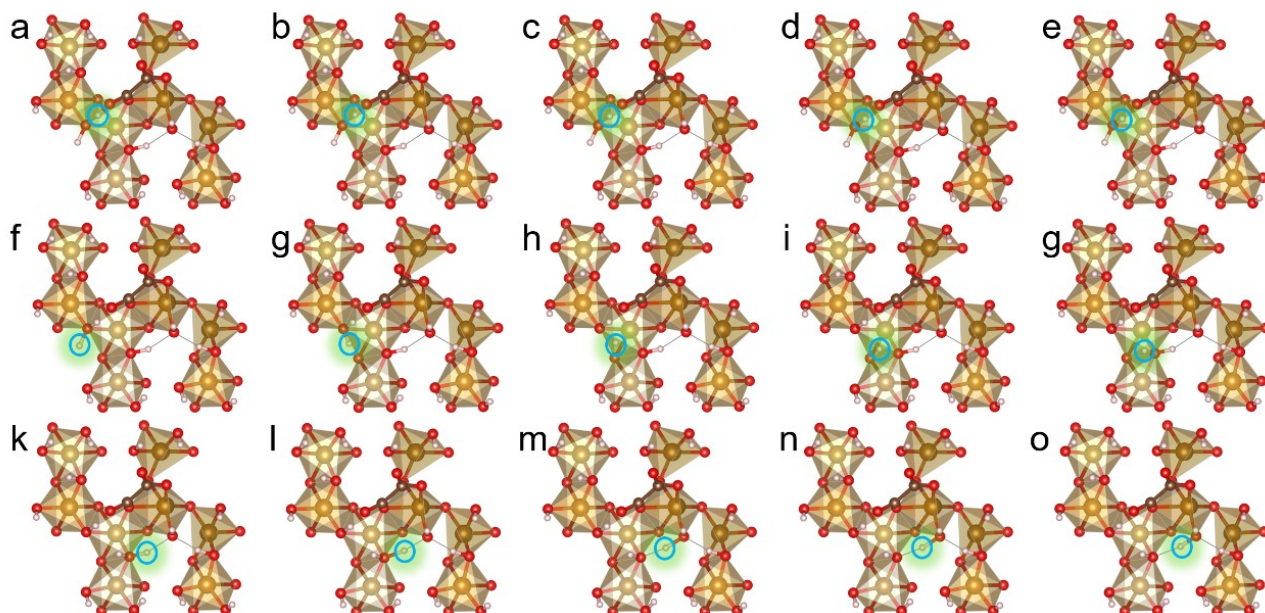


Figure R19. The original structure of HNP {001} adsorbed oxalate during hydrogen transfer process.

The brown polyhedron, red, gray, and white balls represent Fe, O, C, and H atoms, respectively.

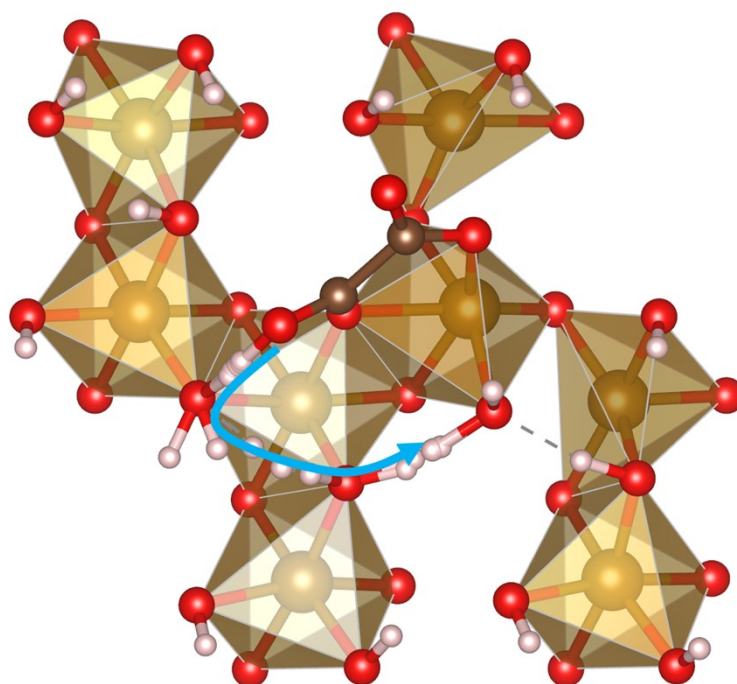


Figure S20. The proton transfer process from adsorbed HC_2O_4^- to the surface hydroxyl group and forming an adsorb-state H_2O on the HNPs surface. The brown polyhedron, red, gray, and white balls represent Fe, O, C, and H atoms, respectively. This Picture overlays multiple snapshots of the hydrogen transfer process of Figure S18 to emphasize the hydrogen transfer path.

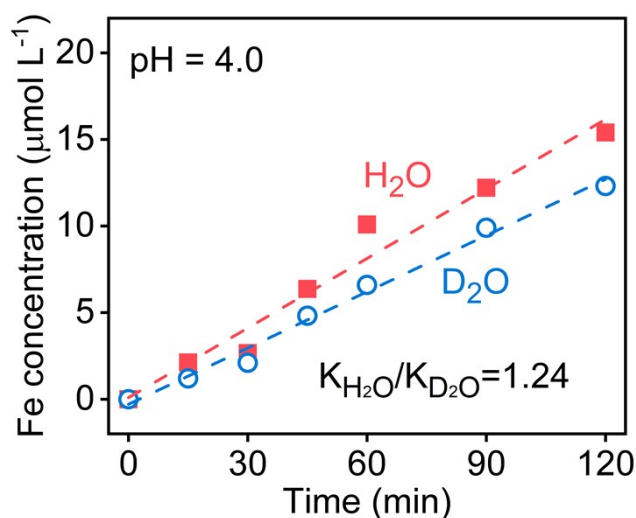


Figure S21. The iron dissolution of HNPs in H_2O and D_2O with 1.0 mmol L^{-1} oxalate at pH 4.0. The dissolution rate of HNPs in H_2O was $40.2 \mu\text{mol L}^{-1} \text{ h}^{-1} \text{ g}^{-1}$, 1.24 times faster than that $32.5 \mu\text{mol L}^{-1} \text{ h}^{-1} \text{ g}^{-1}$ in D_2O under the same condition.

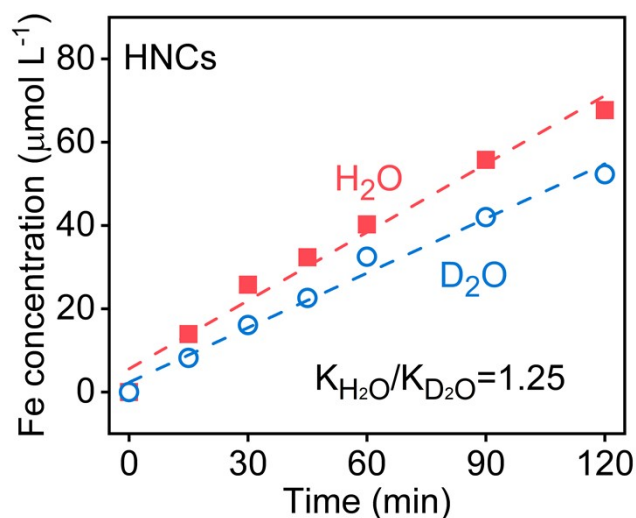


Figure S22. The iron dissolution of hematite nanocubes (HNCs), exposed $\{012\}$ facets, in H_2O and D_2O with 1.0 mmol L^{-1} oxalate at pH 3.0. The dissolution rate of HNCs in H_2O was $164.1 \mu\text{mol L}^{-1} \text{ h}^{-1} \text{ g}^{-1}$, 1.25 times faster than that $131.2 \mu\text{mol L}^{-1} \text{ h}^{-1} \text{ g}^{-1}$ in D_2O under the same condition. The results indicated that hematite of different facets followed the PECT mechanism, despite of possessing different iron dissolution rates.

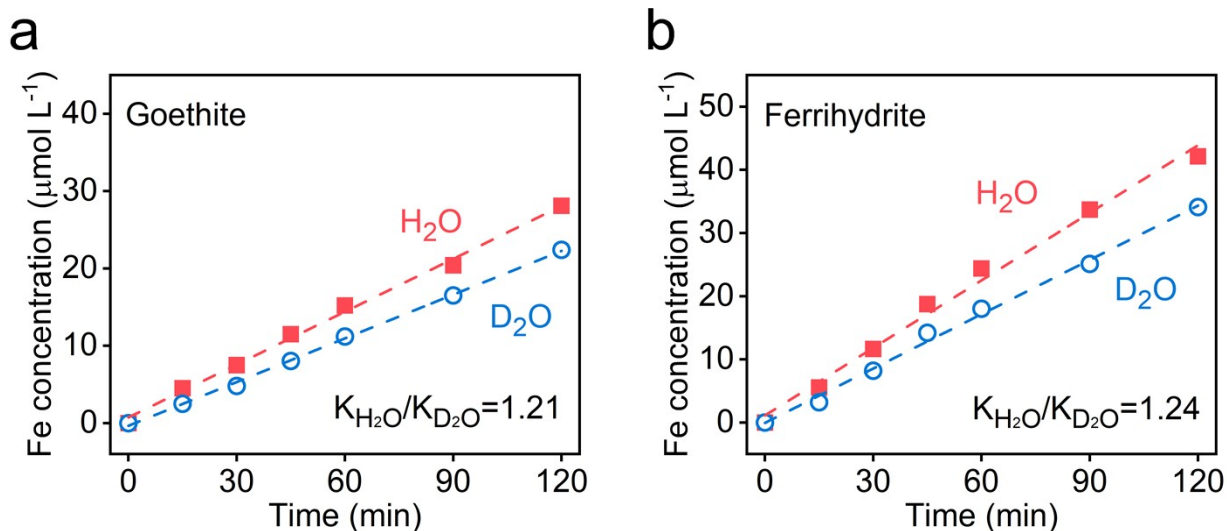


Figure S23. The iron dissolution of goethite (a) and ferrihydrite (b) in H_2O and D_2O with 1.0 mmol L^{-1} oxalate at $\text{pH } 3.0$. The dissolution rate of goethite in H_2O was $68.3 \mu\text{mol L}^{-1} \text{ h}^{-1} \text{ g}^{-1}$, 1.21 times faster than that $56.5 \mu\text{mol L}^{-1} \text{ h}^{-1} \text{ g}^{-1}$ in D_2O under the same condition. And the dissolution rate of ferrihydrite in H_2O was $106.9 \mu\text{mol L}^{-1} \text{ h}^{-1} \text{ g}^{-1}$, 1.24 times faster than that $86.0 \mu\text{mol L}^{-1} \text{ h}^{-1} \text{ g}^{-1}$ in D_2O under the same condition. These kinetic isotope effects of 1.21 and 1.24 were larger than 1, confirming the PCET mechanism of oxalate promoted iron dissolution is universal to other iron (oxyhydr)oxides.

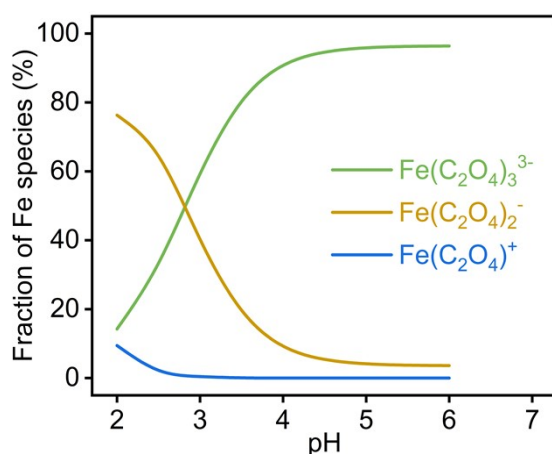


Figure S24. The Fe speciation as a function of pH in 1.0 mmol L^{-1} oxalate and $25 \mu\text{mol L}^{-1}$ Fe(III) solutions. The result revealed that $\text{Fe(C}_2\text{O}_4)_2^{-}$ species dominated around $\text{pH } 2$, while $\text{Fe(C}_2\text{O}_4)_3^{2-}$ species dominated at $\text{pH } 3\text{-}6$ during iron dissolution process.

Table S1. The linear fitted iron dissolution rates and oxalate adsorption capacities of HNPs at various pH. It is worth noting that, Fe(II) was not produced in all iron dissolution experiments.

pH	Dissolution rate ($\mu\text{mol L}^{-1} \text{h}^{-1} \text{g}^{-1}$)		Adsorption capacities ($\text{mmol L}^{-1} \text{g}^{-1}$)
	0 mmol L^{-1} oxalate	1.0 mmol L^{-1} oxalate	
2.0	19.4	65.2	0.66
3.0	0.0	52.2	0.42
4.0	0.0	40.2	0.33
5.0	0.0	19.5	0.21
6.0	0.0	13.6	0.06

Table S2. The linear fitted iron dissolution rates and oxalate adsorption capacities of HNPs at various concentration of oxalate.

Oxalate concentration (mmol L^{-1})	Dissolution rate ($\mu\text{mol L}^{-1} \text{h}^{-1} \text{g}^{-1}$)	Adsorption capacities ($\text{mmol L}^{-1} \text{g}^{-1}$)
0.2	23.5	0.11
0.4	35.2	0.24
0.8	51.3	0.36
1.0	52.2	0.42
1.5	60.7	0.53
2.0	65.5	0.62
4.0	87.9	0.72

Table S3. IR frequencies of adsorbed oxalate on HNPs in ATR-FTIR and Fe-oxalate clusters by simulation.

Stretching Mode	Frequencies (cm ⁻¹)				
	Experimental	DFT-BM	DFT-MM	DFT-MB	DFT-BB
v_s(C=O)	1710	1712 (2)	1617 (-93)	1650 (-60)	1661 (-49)
v_{as}(C=O)	1688	1684 (-4)	1569 (-119)	1534 (-154)	1629 (-59)
v_s(C-O) + v(C-C)	1436	1458 (22)	1510 (74)	1495 (59)	1482 (46)
v_{as}(C-O)	1291	1302 (12)	1328 (37)	1306 (15)	1368 (72)